Numerical modeling of the opening mode fracturing emanating from deformation localization in layered rocks

Alexandre Chemenda, Riad Hassani, Fan Jinyang

To cite this version:

Alexandre Chemenda, Riad Hassani, Fan Jinyang. Numerical modeling of the opening mode fracturing emanating from deformation localization in layered rocks. Computers and Geotechnics, 2022, 147, pp.104774. 10.1016/j.compgeo.2022.104774 . hal-03711737

HAL Id: hal-03711737
https://hal.science/hal-03711737v1

Submitted on 22 Jul 2024

Numerical modeling of the opening mode fracturing emanating from deformation localization in layered rocks

Alexandre I. Chemenda[a], Riad Hassani[a], Jinyang Fan[b]

[a]Université Côte d'Azur, Observatoire de la Côte d'Azur, CNRS, IRD, Géoazur, France

[b]State Key Laboratory of Coal Mine Disaster Dynamics and Control, Chongqing University, Chongqing, 400044, China

Corresponding author:

Alexandre Chemenda (chem@geoazur.unice.fr)

Abstract

It is known that rock fracture includes inelastic straining or damage that should localize at a certain loading stage and result in fracture initiation. The details of this process are not clear, and it is frequently omitted in the models by imposing the initial microcracks (seeds) with certain lengths and orientations. Here we investigate 2-D systems of three layers in finite-difference models. The layers subjected to the horizontal extension are separated by cohesive-frictional interfaces and have contrasted properties typical of sedimentary piles. Fractures are initiated in a more brittle central layer in the vicinity of the interfaces with the adjacent layers. It starts with the initially distributed inelastic straining, which then localized into narrow bands. The damage within these bands is strongly accelerated, resulting in complete material failure locally. Short initial fractures corresponding to narrow bands of failed material are normal to the least local stress. They then propagate from the interfaces to the layer center with further extension. We carefully investigate the impact of different regularization procedures, the grid geometry, and structure on all stages of the fracture process and define the optimal conditions that can be applied for fracture modeling in different structural and loading configurations.

Keywords

Strain localization, pure dilation bands, fracture initiation and propagation, elastoplastic modeling, regularization, layered rocks

1 Introduction

The so-called opening mode (mode I) fractures or joints are the most common in the Earth's crust, notably in sedimentary basins, and frequently form regular sets of vertical (bed-normal) parallel, orthogonal, or more complex fracture networks. They strongly impact the mechanical properties and permeability of rock masses and thereby play an essential role in the stability of geological or man-made structures, production of water and hydrocarbons, storage of CO_2, etc. For this reason, joints have been extensively studied for more than a century (e.g., Pollard & Aydin, 1988) with a particular focus on their spatial distribution in relation to the thickness and mechanical proprieties of fractured sedimentary beds, fracture microstructure, and loading conditions (Price, 1966; Hobbs, 1967; Ji et al., 1998; Huang & Angelier, 1989; Narr & Suppe, 1991; Gross, 1993; Engelder et al., 1997; Bai & Pollard, 2000; Gross et al., 1995; Cherepanov, 1997; Tang et al., 2008; Schöpfer et al., 2011; Li et al., 2012; Guo et al., 2017; Ruf et al., 1998; Rustichelli et al., 2013; Cilona et al., 2016; Levi et al., 2019; Bao et al., 2019; Ji et al., 2021).

The origin of most joints is believed to be related to the mechanical interaction between sedimentary beds that have contrasted lithological and hence mechanical properties and different thickneses (Fig. 1). The conceptual scheme typically used to address and predict the formation of these fractures is shown in Fig. 2. A sedimentary pile (Fig. 2a) is subjected to the horizontal extension, which leads to progressive fracturing (sequential fracture infill) of more brittle (competent) layers and non-localized elastic and/or ductile extension of other (incompetent) layers. The setup of numerical models usually includes only three layers, one competent layer sandwiched between two incompetent ones (Fig. 2b).

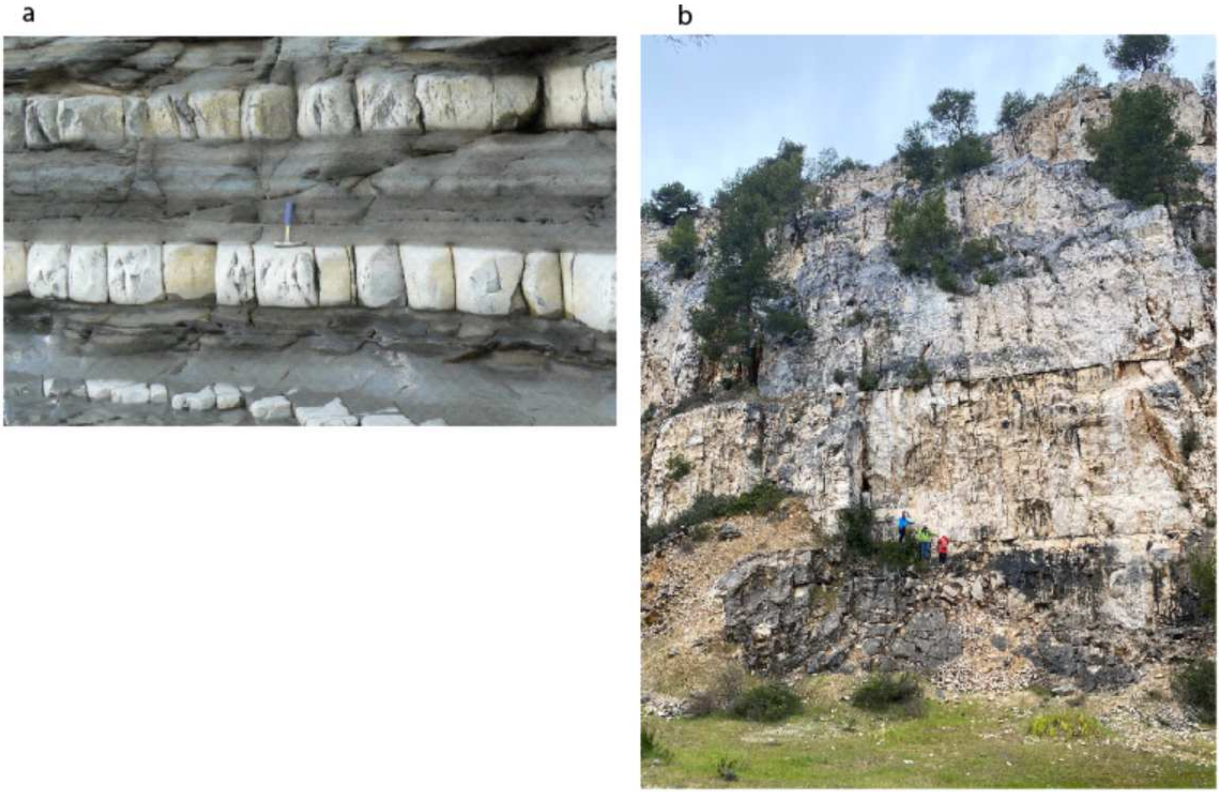

Figure 1. Field examples of layered and fractured sedimentary rocks. (a) Alternating incompetent (mudrocks) and fractured competent (limestone) layers in Lilstock Bay, Somerset, UK (rock hammer for scale) from Schöpfer et al. (2011). (b) Thick densely fractured Urgonian limestone layers; Cassis, Provence, SE France from Chemenda et al. (2021).

In the initial models, the competent layer was elastic, and fracture modeling was based on Linear Elastic Fracture Mechanics (LEFM) (e.g., Gross et al., 1995; Bai & Pollard, 2000). Although LEFM is still dominating in the analysis and modeling of natural fracturing (Bai & Pollard, 2000; Olson et al., 2009; Pollard & Aydin, 1988; Savalli & Engelder, 2005; Segall & Pollard, 1983; Gross et al., 1995; de Joussineau & Petit 2021), it is evident that inelastic deformation is involved in and affects this process. The degree of this involvement depends on the ductility of a fractured material, which in turn depends on its composition, loading conditions (effective pressure), and lithification stage of sedimentary rocks at fracturing (e.g., Paterson & Wong, 2005; Lavenu & Lamarche, 2018; Chemenda, 2019; La Bruna et al., 2020). The elastic-plastic modeling of fracturing was conducted using different numerical methods (Schöpfer et al., 2011; Tang et al., 2008; Li et al., 2012; Guo et al., 2017; Chemenda et al., 2021). The layers in these models were either totally coupled or separated by frictional and/or cohesive interfaces.

A linear relation between the thickness T of the fractured layer and the fracture spacing S has resulted from most modeling studies. The geological data confirm such a relational for $T = T_0 \sim < 1$ m (Engelder et al., 1997; Gross, 1993; Huang & Angelier, 1989; Ji et al., 1998; Narr & Suppe, 1991; Ruf et al., 1998; Rustichelli et al., 2013; Cilona et al., 2016; Levi et al., 2019; Bao et al., 2019). However, for larger T, the $S(T)$ relation becomes very nonlinear so that S practically does not grow with T increase for $T > T_0$ (McQuillan, 1973; Ladeira & Price, 1981; Sagy & Reches, 2006; Ji et al., 2021). This $S(T)$ relation was recently obtained in elastoplastic numerical models (Chemenda et al., 2021), where a progressive fracturing in the initially homogeneous models resulted from inelastic straining or damage of the material. At a certain stage, the damage localizes into narrow pure dilation deformation bands, leading to complete material failure that is fracture initiation. This process can involve the whole layer if T is sufficiently small, or only the parts near the interfaces with the adjacent layers if T is large. In the latter case, the fracture develops in two stages. The first one includes distributed layer damage in the vicinity of its horizontal boundaries, localization of this damage in bands, and fracture initiation. At the second stage, the initiated fracture propagates quasi-statically across the layer. These processes are the subject of a detailed study in this paper.

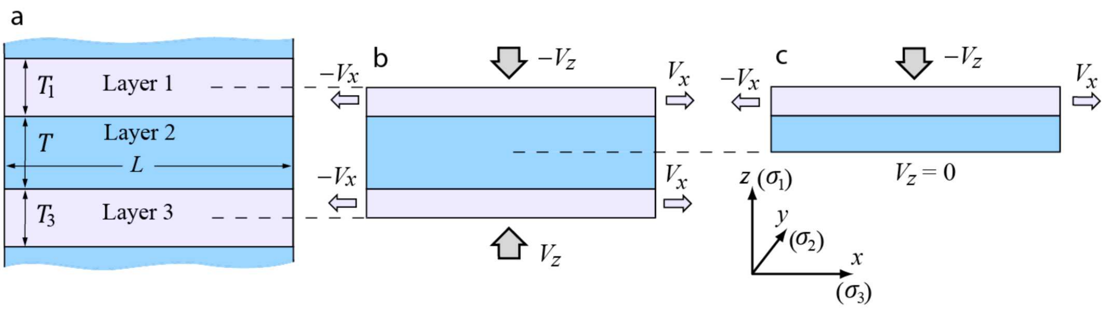

Figure 2. Setup of 3-layer models. (a) Series of alternating incompetent (pink) and competent (blue) layers. (b) An elementary (repeating) element of this series which corresponds to the

complete three-layer modeling setup. (c) A half-symmetry modeling setup, with thicknesses of layers 1 and 2 being $T_1/2$ and $T/2$, respectively. V_x and V_z are the velocities applied in the corresponding directions to layers 1 and 3. V_x causes deformation and fracturing of layer 2 and V_z is to maintain constant average vertical (lithostatic) stress at the horizontal model boundaries. The y-normal model boundaries are fixed in the y-direction. The layers are separated by cohesive-frictional interfaces. The models are pre-stressed in the y- and z-directions as indicated below. Layers 1 and 3 are purely elastic and layer 2 is elastoplastic. $T_1 = T_1 = 0.2$ m, $T = 1$ m, and $L = 0.6$ m.

Since fractures emanate from dilation localization bands, strain localization is a fundamental element of fracture formation and should be accurately modeled. This process, resulting from a constitutive instability and deformation bifurcation (Rice, 1976; Rudnicki & Rice, 1975), is known to be strongly mesh-dependent in continuum numerical models (e.g., Needleman, 1988; Pijaudier-Cabot & Bažant, 1987), and therefore requires their regularization to reduce the mesh dependence. In Chemenda et al. (2021), the reduction of mesh-dependence of the modeling results was achieved by integrating the mesh size Δz into the constitutive formulation so that the energy dissipation within the deformation/fracture bands is independent on Δz. Since this procedure does not eliminate the ill-posedness of the initial value problem during strain localization, the numerical scheme used might not be robust enough to capture correctly the deformation banding that affects the following fracture process. Different regularization techniques have been applied to deal with this issue, including nonlocal/gradient (e.g., Chen & Schreyer, 1987; Needleman, 1988; Nguyen & Korsunsky, 2008; Pijaudier-Cabot & Bažant, 1987; Poh & Swaddiwudhipong, 2009; Vardoulakis, 1989) or viscous (Duvaut and Lions, 1972; Perzyna, 1996; Needleman, 1988; Simo et al., 1988; Wang et al., 1997; Loret and Prevost, 1990) elastoplastic models. Viscous regularization is the simplest, not expensive numerically, and widely used approach (e.g., Das et al., 2013; Carosio et al., 2000; Heeres et al., 2002; Shahin, et al., 2019; Duretz et al., 2019), which is also applied here.

Below we describe the constitutive model and the regularization aphorisms used. We then present the mentioned above main three-layer (Fig. 2) and subsidiary, one-layer modeling setups. The latter is designed to investigate the details of dilation banding for different model parameters. We then present and discuss the modeling results obtained and give our conclusions.

2 Constitutive model

To model inelastic straining and fracture of layer 2 (Fig. 2), we use the constitutive model from Chemenda et al. (2021) summarized here. The model includes the following composite yield function

$$F = \begin{cases} F_t = \sigma_t + \sigma_3 & if\ \sigma_1 \leq \sigma_{int} \\ F_s = \alpha_c \sigma_3 + \sigma_c - \sigma_1 & if\ \sigma_1 > \sigma_{int} \end{cases} \tag{1}$$

where F_t and F_s are the yield functions for the tensile and shear failure mechanisms, respectively; σ_t and σ_c are the tensile and unconfined compression strengths, respectively; σ_{int} is the abscise of the intersection point of the envelopes $F_t = 0$ and $F_s = 0$ in the $(\sigma_1, \sigma_3, \varepsilon^p)$ coordinates (Fig. 3), where ε^p is the accumulated inelastic volume strain tracking the history of inelastic strain. A rock mechanics convention is used for stresses: $\sigma_1 \geq \sigma_2 \geq \sigma_3$, where the compressive stress is positive, and tension is negative. All stresses are effective. The parameters σ_t, σ_c, and σ_{int} are functions of ε^p

$$\sigma_t(\varepsilon^p) = \sigma_t^0 \kappa(\varepsilon^p),\ \ \sigma_c(\varepsilon^p) = \sigma_c^0 \kappa(\varepsilon^p),\ \ \sigma_{int}(\varepsilon^p) = \sigma_{int}^0 \kappa(\varepsilon^p) \tag{2}$$

where ε^0 is the ε^p value at which both tensile and compression strengths reach zero during failure; $\kappa(\varepsilon^p) = \max(0, (1 - \varepsilon^p/\varepsilon^0))$; σ_t^0, σ_c^0, and σ_{int}^0 are the initial (at $\varepsilon^p = 0$) values of σ_t, σ_c, and σ_{int}; α_c is the dimensionless material (friction) parameter related to the Coulomb internal friction angle φ as

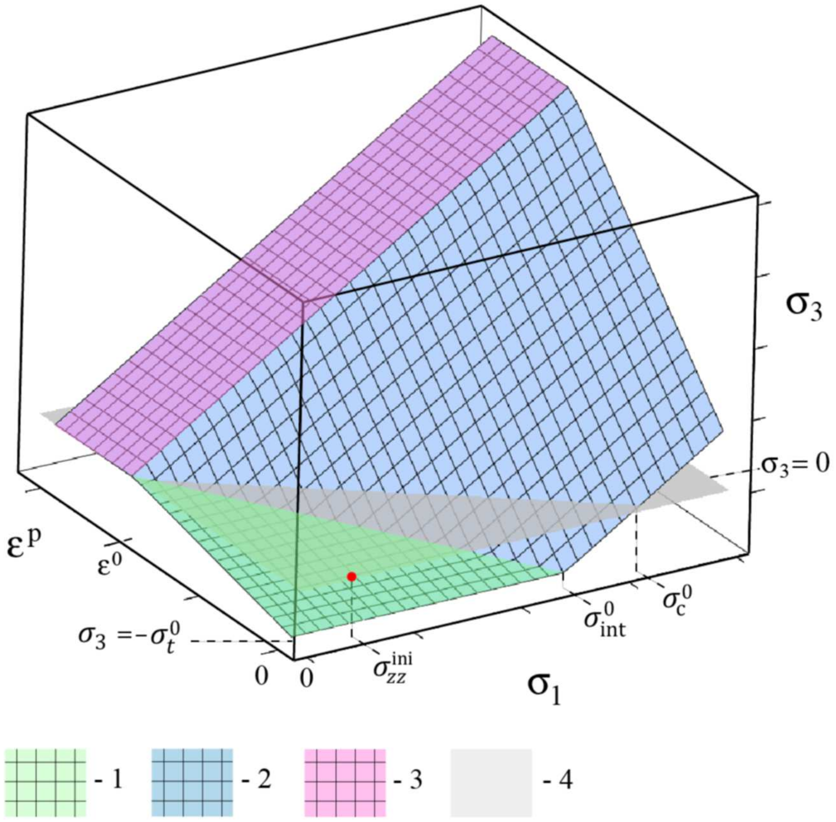

$$\alpha_c = \frac{1+\sin(\varphi)}{1-\sin(\varphi)}. \tag{3}$$

Figure 3. Composite yield surface $\sigma_3(\sigma_1, \varepsilon^p)$. (1) Tensile failure. (2) Shear failure. (3) Post failure (after complete failure). (4) Shows a zero-level of σ_3. The red point (circle) corresponds to the initial stresses $\sigma_1 = \sigma_{xx}^{ini}$ and $\sigma_3 = 0$ applied to the models.

The tensile and shear failure mechanisms are thus coupled in this model by synchronous evolution of the strengths σ_t and σ_c during the inelastic straining; both reach zero at the same ε^p, $\varepsilon^p = \varepsilon^0$ (Fig. 3).

The plastic potential function Φ reads

$$\Phi = \begin{cases} \Phi_t = \sigma_3 & if\ \sigma_1 \leq \sigma_{int} \\ \Phi_s = \beta_c \sigma_3 - \sigma_1 & if\ \sigma_1 > \sigma_{int} \end{cases} \tag{4}$$

where Φ_t and Φ_s are the plastic potentials for the tensile and shear failure mechanisms, respectively; β_c is the material coefficient depending on ε^p and linearly decreasing from its initial value β_c^0 to 1 with ε^p

$$\beta_c = \beta_c^0 + (1-\beta_c^0)(1-\kappa) \tag{5}$$

This coefficient defines the dilatancy factor $\beta = d\varepsilon^p/d\bar{\gamma}^p$, where $d\bar{\gamma}^p$ is the increment of inelastic equivalent or maximum shear strain. For the latter case

$$\beta = \frac{\beta_c - 1}{\beta_c + 1}. \tag{6}$$

as can be obtained from (4, 5) and the flow rule

$$d\varepsilon_i^p = d\lambda \frac{\partial \Phi_s}{\partial \sigma_i}, \tag{7}$$

where $d\lambda$ is the nonzero scalar function ($d\lambda$ is different for the different failure mechanisms introduced), $i = 1,2,3$. It follows from (6) that when $\beta_c = 1$, $\beta = 0$. We assume here that $\beta_c^0 = 1$, meaning no inelastic volume increase (change) during inelastic shear deformation. This increase can occur only when the tensile failure/damage mechanism is activated.

2.1 Integration of the mesh size into the constitutive formulation

To deal with the mesh-dependence of the results of fracture modeling, the mesh (numerical zone) size Δz is related to ε^0 as (Chemenda et al., 2021)

$$\varepsilon^0 = \tilde{\varepsilon}^0 (\frac{C}{\Delta z}) \tag{8}$$

where C is a constant coefficient, and $\tilde{\varepsilon}^0$ is equal to ε^0 when $\Delta z = C$. This relation allows reducing the dependence on Δz of the rate of inelastic energy dissipation W within the deformation/fracture band during its extension. Indeed, as follows from (Eqs. 4 and 7), only the σ_3-parallel component of inelastic strain is nonzero and is equal to ε^p during the tensile failure. Assuming that inelastic straining within the band is uniform, that the band width d_0 is proportional to Δz ($d_0 \sim \Delta z$), and $\varepsilon^p = \Delta d / d_0 \sim \Delta d / \Delta z$, the energy dissipation rate W per unit height and thickness of the band can be written as

$$W = \frac{d_0}{\Delta d}\int_0^{\varepsilon^p} \sigma_t(\,\varepsilon^p)d\varepsilon^p \sim \frac{\Delta z}{\Delta d}\int_0^{\Delta d} \sigma_t\left(\frac{\Delta d}{\Delta z}\right)\frac{\mathrm{d}(\Delta d)}{\Delta z} = \sigma_t^0\left[1-\frac{\Delta d}{2\Delta z \varepsilon^0}\right] \qquad (9)$$

W will be constant for a given Δd when $\Delta z \varepsilon^0$ is constant, which is equivalent to (8).

2.2 Viscous regularization

The procedure described above does not eliminate the loss of hyperbolicity or ellipticity of the field equations in dynamic or static regimes, respectively, which results in the ill-posedness of the initial value problem during instability leading to strain localization. To tackle this problem, we introduce viscosity into the constitutive formulation using Duvaut-Lions scheme (Duvaut and Lions, 1972) investigated notably by Loret and Prevost (1990). The resulting constitutive relations in small strain formalism read

$$\begin{aligned} \dot{\sigma}_{ij} &= 2G\dot{\varepsilon}_{ij} + \left(K - \tfrac{2}{3}G\right)\dot{\varepsilon}_{kk}\delta_{ij} - \tfrac{1}{\eta}(\sigma_{ij} - \bar{\sigma}_{ij})H\left(F(\sigma_{ij}, \varepsilon^p)\right) \\ \dot{\varepsilon}^p &= -\tfrac{1}{\eta}(\varepsilon^p - \bar{\varepsilon}^p)H\left(F(\sigma_{ij}, \varepsilon^p)\right) \end{aligned} \qquad (10)$$

where σ_{ij} and ε_{ij} are the stress and strain tensors, respectively; $(\dot{\ })$ and $(\bar{\ })$ denote respectively the time derivative and the solutions of the inviscid problem; G and K are the shear and bulk elastic moduli, respectively; H is the Heaviside step function, and $\eta \geq 0$ is the nonnegative parameter with the dimension of time, called the relaxation time; $i, j, k = 1,2,3$. For $\eta = 0$, the rate-independent plasticity model is recovered $(\sigma_{ij}, \varepsilon^p) = (\bar{\sigma}_{ij}, \bar{\varepsilon}^p)$.

We have implemented the constitutive model (1, 2, 4, 5, 8, 10) into the finite-difference dynamic time-marching explicit code FLAC3D (Itasca, 2021), used in a quasi-static mode (i.e., the steady-state solution of a fully dynamic problem is obtained by a dynamic relaxation method). In our implementation, we use the discrete approximation given by Simo et al. (1988), which can be summarized in the following steps. Assuming a constant strain increment $\Delta\varepsilon_{ij} = \varepsilon_{ij}\Delta t$ over the time interval $[t^n, t^n + \Delta t]$ between steps n and $n + 1$, we compute the elastic trial stress

$$\sigma_{ij}^{tr} = \sigma_{ij}^{n} + 2G\Delta\varepsilon_{ij} + \left(K - \tfrac{2}{3}G\right)\Delta\varepsilon_{kk}\delta_{ij} \qquad (11)$$

If $F(\sigma^{tr}, \varepsilon^{pn}) < 0$, $\left(\sigma_{ij}^{n+1}, \varepsilon^{pn+1}\right) = \left(\sigma_{ij}^{tr}, \varepsilon^{pn}\right)$, otherwise the inviscid back-bone solution $\left(\bar{\sigma}_{ij}^{n+1}, \bar{\varepsilon}^{pn+1}\right)$ is first computed by projecting the stress state onto the current yield surface. Then (10) is integrated using the Euler backward scheme to obtain the visco-elastoplastic solution (update/correction of σ_{ij} and ε^{p}).

$$\sigma_{ij}^{n+1} = \tfrac{1}{1+\gamma}\left(\sigma_{ij}^{tr} + \gamma\bar{\sigma}_{ij}^{n+1}\right), \quad \varepsilon^{pn+1} = \tfrac{1}{1+\gamma}\left(\varepsilon^{pn} + \gamma\bar{\varepsilon}^{pn+1}\right) \qquad (12)$$

where the only new parameter is $\gamma = \Delta t/\eta$. This dimensionless nonnegative parameter influences the inelastic deformation in an opposite way to the classical viscosity coefficient. The viscosity effect is maximum when $\gamma \to 0$, and $\gamma = 0$ corresponds to purely elastic behavior. The viscosity effect is inexistent when $\gamma = \infty$, which corresponds to a purely elastoplastic or inviscid model.

2 Modeling setup

2.1 Three-layer models

As in the previous studies cited in the Introduction, we investigate a three-layer model shown in Fig. 2b. Layers 1 and 3 are subjected to the horizontal extension, generating shear stresses at the layer interfaces driving the extension and fracturing of the central layer 2. This layer has free vertical boundaries that can be considered preexisting, previously formed fractures. The whole model is pre-stressed to the initial stresses σ_{zz}^{ini}, σ_{yy}^{ini}, and σ_{xx}^{ini}. The horizontal extension applied to the model causes its vertical shortening. To maintain the average vertical stress constant and equal to σ_{zz}^{ini}, we apply servo-controlled vertical velocities V_z to the horizontal boundaries of the models (Fig. 2b).

The layers are connected by frictional and cohesive interfaces whose shear strength τ_0^{int} is defined by the interface friction coefficient μ^{int} and cohesion c^{int}

$$\tau_0^{int} = \mu^{int}\sigma_n + c^{int} \tag{13}$$

where σ_n is the effective normal to interface stress which is equal to the normal vertical stress σ_{zz}. The normal (k_n) and shear (k_s) stiffnesses of the interfaces are set to (Itasca, 2021)

$$k_n = k_s = 10\max\left[\frac{4G+3K}{3\Delta z}\right] \tag{14}$$

where "max" means that the maximum value over all zones adjacent to the interface is to be used.

Fig. 2b shows the complete modeled structure, but to reduce the calculation time, the simulations have been carried out with the half-symmetry setup in Fig. 2c.

2.2 One-layer models

Before three-layer modeling, we investigate the setup in Fig. 4a with one elastoplastic layer subjected to the uniaxial extension. These models with simple geometry and uniform loading and straining conditions correspond to the theoretical framework of the analysis of deformation localization (bifurcation) that results from a constitutive (or material) instability (Rice, 1976). They are designed to investigate this phenomenon in a specific regime corresponding to pure dilation banding and to compare the results against the relevant theoretical predictions (Ottosen & Runesson, 1991). Particular attention is given to understanding the impact of the regularization algorithms presented on strain localization and studying the influence of the numerical grid geometry and structure shown in Figs. 4b–4d on the localization. The double sheet brick-wedge grid in Fig. 4d consists of the attached brick- and wedge-shaped grids shown in Figs. 4b and 4c. The attachment procedure consists of a rigid attachment (or slaving) of the gridpoints of one zone to the opposite, master gridpoints, faces, or edges by imposing to the slave gridpoints of velocities/displacements obtained from those in the three or four grid points that make up the master face. Forces are distributed from the slave to the master gridpoints. The velocities obtained from the equations of motion at each step are transferred from the master to the slave gridpoints using weighting values (Itasca, 2021).

When the layer model has a strictly rectangular (parallelepipedal) shape and uniform properties, its extension leads to the formation of pure dilation deformation bands along one or both vertical borders. A small zone of a very small weakness is usually imposed at the model center to avoid these boundary effects. Another way, which we preferred in this study, is a very small progressive (sinusoidal) thinning of the model (plate) with the maximum amplitude of 1 μm in its central part.

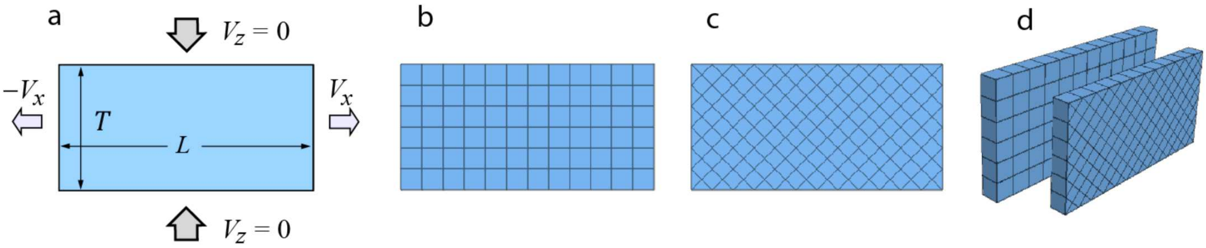

Figure 4. Setup of one-layer models (a) and grid geometries used (b to d). (b and c) Brick- and wedge-shaped grids, respectively. (d) Double-layer sheet grid, with the attached brick and wedge-shaped grids. $T = 0.1$ m, and $L = 0.2$ m.

3 Modeling results

The results are organized below into five groups addressing different aspects of strain localization and fracture. The first four groups include one-layer models (setup in Fig. 4a), and the two next ones present three-layer models (Fig. 2b) run using a half-symmetry setup in Fig. 2c.

The deformation localization and fracture patterns are shown in terms of the tensile strength σ_t. When σ_t is equal to its initial value $\sigma_t^0 = 7$ MPa, there is no material damage, and when $\sigma_t = 0$, the material is wholly fractured/failed. The case $0 < \sigma_t < \sigma_t^0$ corresponds to the dilatant damage of the material. Localization of such damage within a narrow band corresponds to pure dilation banding, which can evolve to fracture with the following damage accumulation. Since the only elastoplastic layer (layer 2 in Fig. 2) can fracture, only this layer is shown in the figures presenting the results from 3-layer models.

The deformation stages are characterized by the nominal normal horizontal extension strain $\varepsilon_{xx} = -\Delta L/L$, where L is the model length, and ΔL is its horizontal lengthening. In 1-layer models, ε_{xx} (or more precisely, V_x) is applied to the vertical borders of the layer (Fig. 4a), and in 3-layer models, only to layers 1 and 3 (Fig. 2b). The nominal horizontal stress σ_{xx} in the stress-strain curves presented below for 1-layer models is the average over the layer thickness normal stress in the x-direction.

We use here the model parameter values assumed and justified in Chemenda (2019) and Chemenda et al. (2021). The parameter values common for all models are $E = 20$ GPa; $\nu = 0.25$; $\sigma_c^0 = 60$ MPa, $\sigma_t^0 = 7$ MPa, $\alpha_c = 3$, $\beta_c^0 = 1$, $C = 0.1$ m, $\rho = 2600$ kg/m^3, $\sigma_{zz}^{ini} = 10$ MPa, $\sigma_{yy}^{ini} = \sigma_{zz}^{ini}/2$. In 1-layer models: $L = 0.2$ m, $T = 0.1$ m, $V_x = 1 \times 10^{-10}$ m/s, and $\sigma_{xx}^{ini} = -6.97$ MPa, which is set close to $-\sigma_t^0$ to approach the failure point and reduce the time for the purely elastic loading. For 3-layer models: $T_1 = T_3 = 0.2$ m, $T = 1$ m, $L = 0.6$ m (see Fig. 2a for definitions), $c^{int} = \tau_0^{int} = 4$ MPa, $k_\mathrm{n} = k_\mathrm{s} = 9.6 \times 10^{12}$ Pa/m (calculated from (14)), $\sigma_{xx}^{ini} = 0$, $V_x = 5 \times 10^{-9}$ m/s. Other parameters: Δz, ε^0, and γ, are varied in the models of different groups and are given in the captions of corresponding figures. For the chosen $\sigma_{zz}^{ini} = \sigma_1$ value, inelastic straining starts in the tensile failure domain, as can be seen in Fig. 3 (red circle). Therefore, the localization of strain (damage) should occur at negative hardening modulus (which is the case in our models) in the form of pure dilation bands oriented normal to σ_3 (Ottosen & Runesson, 1991; Chemenda, 2019).

Given that stresses are effective and assuming that the pore pressure is equal to the hydrostatic pressure, the lithostatic stress σ_{zz}^{ini} is related to the depth z as

$$\sigma_{zz}^{ini} = (\rho - \rho_w)gz = 640 \text{ m} \tag{15}$$

where $\sigma_{zz}^{ini} = 10$ MPa, $\rho_w = 10^3$ kg/m^3 is the water density, and g is the acceleration of gravity.

3.1 Pure dilation banding in a layer under uniaxial horizontal extension

Group 1: Impact of the viscosity parameter γ on the initiation and evolution of strain localization.

Fig. 5 shows five deformation stages (columns 1 to 5) in three models (lines a to c) for different γ, decreasing from a to c. One can see that the higher the viscosity (the lower the γ value), the slower the strain localization and the wider the dilation bands at the initial stages of their evolution. There is, however, no fundamental difference between the models and the width d_0 of final band/fracture zones (column 5): it is practically the same and equal to $\sim\Delta z$. As expected, the deformation bands are normal σ_3 (horizontal in Fig. 5) and hence parallel to σ_1, which is vertical in the figure. Therefore, the obtained deformation bands are pure dilation bands, which is also confirmed by the orientation of the velocity field within them.

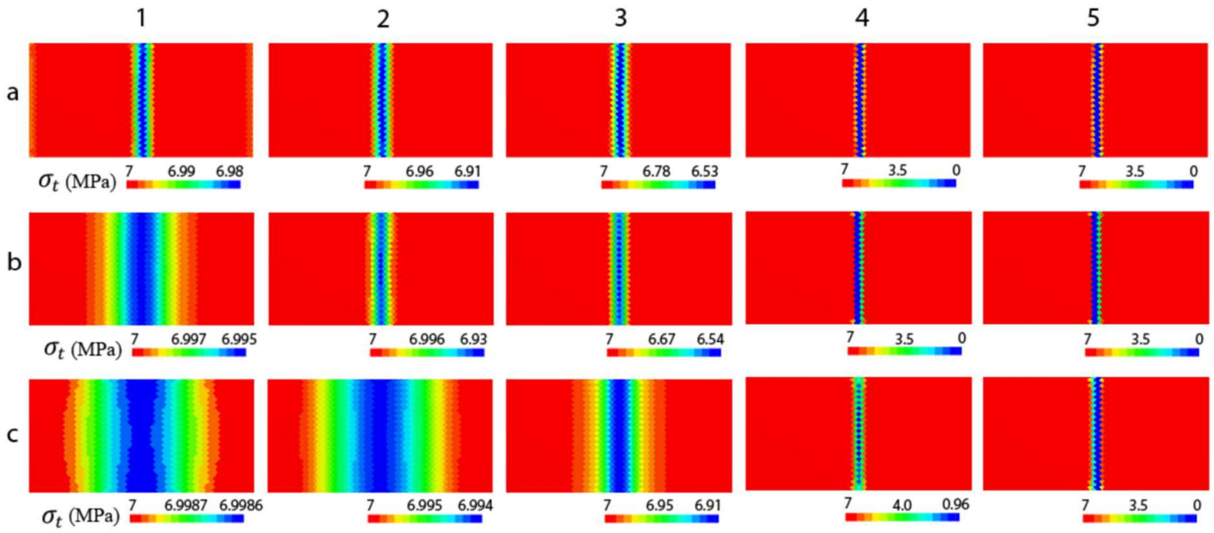

Figure 5. Group 1. Evolution of strain localization and fracture (stages/columns 1 to 5) in three models (a to c) differing only by the γ value: in (a), $\gamma = \infty$; in (b), $\gamma = 0.1$, and in (c), $\gamma = 0.01$. Deformation stages 1 to 5 correspond to ε_{xx} equal to -5×10^{-6}, -1.5×10^{-5}, -6×10^{-5}, -4.5×10^{-4}, and -7.8×10^{-4}, respectively. $\Delta z = 5$ mm and $\varepsilon^0 = 0.02$. All the models have wedge-shaped grids shown in Fig. 4c.

Group 2: Dependence of the dilation banding and fracture on the grid geometry and resolution in the inviscid and viscous models

Fig. 6 shows the final stages of strain localization corresponding to the complete failure of the material in ten models with brick- (Figs. 6a) and wedge- (Figs. 6b) shaped meshes with different resolutions specified in the figure caption. The models in columns 1 and 2 are inviscid ($\gamma = \infty$), and in the models in columns 3 to 5, $\gamma = 1 \times 10^{-3}$. In the inviscid models, the deformation/fracture band width d_0 is equal to $\sim\Delta z$. In the viscous models (columns 3–5), d_0 includes several grid elements. Their number increases with the Δz reduction so that d_0 remains constant (Δz $-$independent) for sufficiently small Δz, $\Delta z < \sim 4$ mm. Therefore, the introduction of sufficiently small γ (large viscosity) regularizes the problem in the sense that d_0 becomes independent of both the grid resolution and geometry. This is true not only for the brick- and wedge- (compare images in columns 4 and 5), but also for double brick-wedge grids shown in Fig. 4d. The structural stress-strain responses also converge with Δz reduction

(Fig. 6g), although they are different for different grids (Figs. 6h). The $\sigma_{xx}(\varepsilon_{xx})$ curves for the inviscid models are different (Figs. 6c to 6e) and attest to more brittle behavior, with the brittleness increasing as Δz decreases (compare Figs. 6d and 6e).

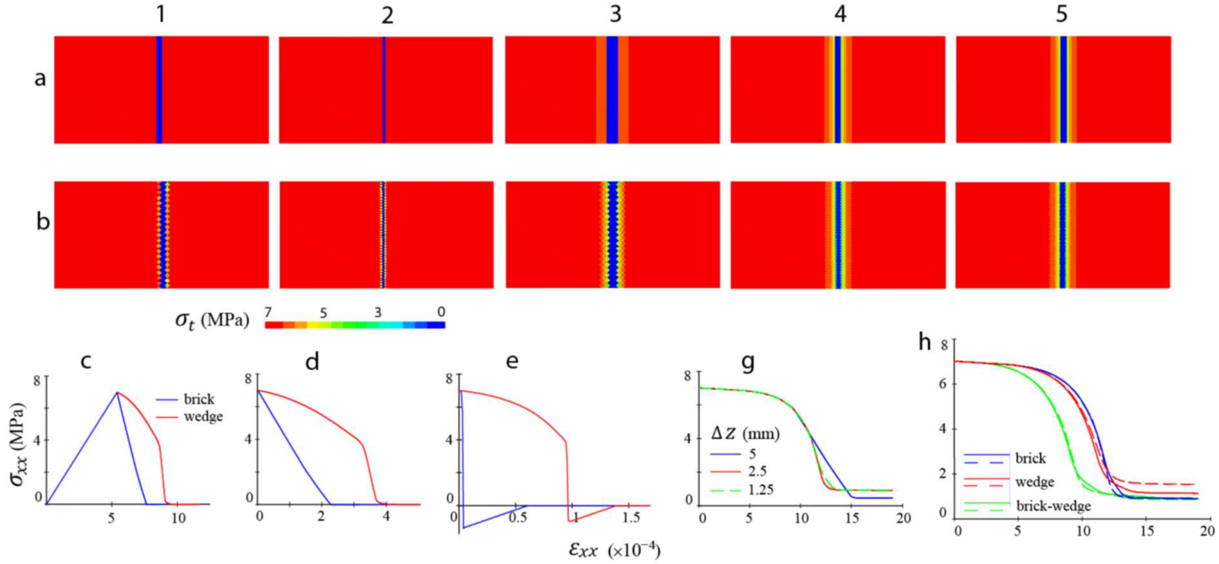

Figure 6. Group 2. Impact of the grid geometry, resolution, and the regularization parameter γ on the dilation banding and structural stress-strain response. Final stages of strain localization and fracture are shown for five models with brick- (a) and wedge-shaped (b) meshes, respectively. The resolution of the models in columns 1 and 3 is $\Delta z = 5$ mm, in columns 2 and 4, 2.5 mm, and in column 5, 1.25 mm. In columns 1 and 2, $\gamma = \infty$, and in columns 3 to 5, $\gamma = 1 \times 10^{-3}$. (c to h) Nominal stress-strain curves $\sigma_{xx}(\varepsilon_{xx})$ in the presented models. Since the models are prestressed to σ_{xx} close to $-\sigma_t^0$, the curves start near the initial failure (yield) point except in (c), where the elastic loading stage (segment) is added to the curves in (d). The curves in (d and e) are respectively for the models in columns 1 and 2 (curve (c) is for column 1 as well). Curves in (g), are for the regularized brick-shaped models in (a3 to a5) with different resolutions indicated on the plot. (h) Curves for the regularized models with the brick, wedge, and double brick-wedge grids corresponding to the curves of different colors as indicated in (h). Solid curves are for $\Delta z = 1.25$ mm, and the dashed ones, for $\Delta z = 2.5$ mm.

Group 3: Impact of the grid geometry on the orientation of deformation bands and the resulting fractures.

The pure dilation bands in our models (given the constitutive framework used and the stress values applied) should form normal to σ_3 and parallel to σ_1 and σ_2. However, the grid geometry can also affect the band orientation (as well as its width) in the numerical models. When σ_1 is parallel to a grid line, the band is parallel to this line as can be seen in Fig. 7a1 (all models in Fig. 7a have brick-shaped meshes shown in Fig. 4b). The dilation bands and resulting fracture bands remain parallel to the grid line (vertical in Fig. 7), even when the σ_1 orientation deviates from this line provided that the deviation angle ψ does not exceed a certain value. In Fig. 7a2, $\psi = 15°$, but the final deformation/fracture band is still vertical. In Fig. 7a3, $\psi = 30°$ and the band is inclined (but not parallel to σ_1). In this case d_0 is ~$1.5\Delta z$, whereas in Figs 7a1 and Figs 7a2 where the bands are parallel to the grid lines, $d_0 = \Delta z$. It was expected that in the regularized models, the orientation of the fracture bands would be closer to σ_1; however, this is not the case (Fig. 7a4). Similar conclusions can be drawn from the models in Figs. 7b with wedge-shaped grids. On the contrary, the models with the double-layer grids provide more satisfactory results (Fig. 7c) both in terms of the band thickness (which is practically the same, $d_0 \approx 1.5\Delta z$, for different ψ) and orientation. This orientation further approaches that of σ_1 with the mesh refinement.

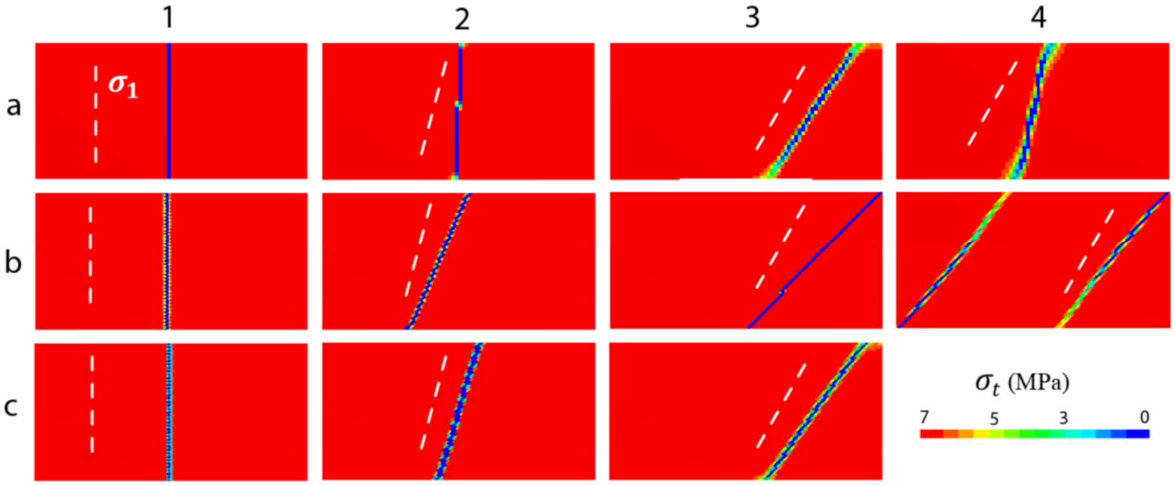

Figure 7. Group 3. Final stages of strain localization and fracture in the models with brick (a), wedge (b), and double brick-wedge (c) grids. The columns 1 to 3 correspond to different orientations of the initial stress axes defined by angle ψ between σ_1 (shown by the white dashed lines) and the vertical; ψ is 0°, 15°, and 30° in columns 1, 2, and 3, correspondingly. In column 4, $\psi = 30°$. The rotation of the initial stress axes is achieved by imposing the

corresponding normal and shear initial and boundary stresses. Models in columns 1 to 3 are inviscid ($\gamma = \infty$), and in column 4, $\gamma = 1 \times 10^{-3}$. In all models $\Delta z = 2.5$ mm and $\varepsilon^0 = 0.02$.

The presented results show that although the viscous models exhibit clear regularization effects on the strain localization and band formation, they do not provide satisfactory results on the geometry and orientation of the fracture bands (Fig. 7a4 and 7b4) or the stress-state during and after the fracture formation. Indeed, the residual viscous horizontal tensile stress after the complete fracture (complete material failure) is $\sigma_{xx} \approx -1.2$ MPa on average in Fig. 6h, whereas it should be zero in reality. The magnitude of this stress can be reduced by decreasing the viscous effect, i.e., by increasing γ. However, the increase of γ requires a rapid growth of the model resolution (reduction of Δz) to achieve a stabilization of both d_0 and the stress-strain response. For example, for $\gamma = 1 \times 10^{-3}$ applied in the models in Figs. 6a3–6a5 and b3–b5, the stabilization starts at $\Delta z \approx 4$ mm, whereas for $\gamma = 1 \times 10^{-2}$ (still corresponding to high viscosity) it occurs at $\Delta z \approx 0.8$ mm. Such resolution is too high for most real-life applications. The viscous effects become negligible at much larger γ, $\gamma \approx 10$ as seen hereafter (Fig. 8f). This increases the attractivity of using the double-layer grid in Fig. 4d with sufficiently large γ (low viscosity) needed only to ensure the well-posedness of the initial value problem. In this case, one has to give up the convergence of d_0 to a certain value that in any case cannot be realistic (very small), as will be discussed below. To ensure the independence of the energy dissipation on Δz within deformation bands during fracture, ε^0 should be related to Δz by Eq. (8). This has been done in the models of the next group.

Group 4: Dilation banding and fracture in a layer in the models with different ε^0 (or hardening modulus) and Δz.

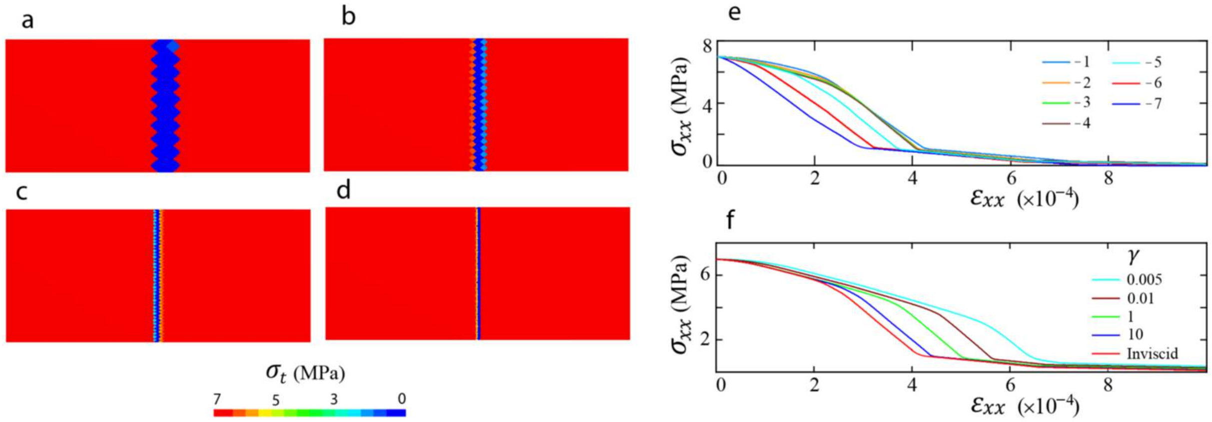

Figure 8. Group 4. (a to d) Final stages of strain localization and fracture in the inviscid models with double brick-wedge grids and different ε^0 and Δz related by Eq. (8): (a) $\varepsilon^0 = 0.01$ and $\Delta z = 10$ mm; (b) $\varepsilon^0 = 0.02$ and $\Delta z = 5$ mm; (c) $\varepsilon^0 = 0.04$ and $\Delta z = 2.5$ mm; (d) $\varepsilon^0 = 0.08$ and $\Delta z = 1.25$ mm. (e) Nominal stress-strain curves from the models presented and other similar ones with different Δz (and hence ε^0): for (1) $\Delta z = 0.625$ mm; (2) $\Delta z = 1.25$ mm; (3) $\Delta z = 2$ mm; (4) $\Delta z = 2.5$ mm; (5) $\Delta z = 2.7$ mm; (6) $\Delta z = 5$ mm; (7) $\Delta z = 10$ mm. (f) Nominal stress-strain curves obtained from other models with $\Delta z = 1.25$ mm, $\varepsilon^0 = 0.08$, and different γ indicated on this figure.

Figs. 8a–d show the fracture bands resulting from strain localization and evolution of pure dilation deformation bands in the double brick-wedge-grid models with different Δz and ε^0 related by Eq. (8). As expected, the final band thickness d_0 decreases linearly with the Δz decrease. On the contrary, the stress-strain curves in Fig. 8e become very close for $\Delta z < 2.5$ mm. These models are inviscid, i.e., $\gamma = \infty$. Reduction of γ, leads to the increase in the viscous stresses, reduction of the average viscoplastic hardening modulus (Fig. 8f), and increase in the dissipation energy. All these effects become negligible when γ is sufficiently large, larger than ~10 (Fig. 8f). For such γ values, the evolution of strain localization and fracture is practically the same as in the inviscid models. For smaller γ, the localization of deformation is more progressive, as can be seen in Fig. 5, and will be demonstrated below in the models of group 6. The models of this group and those of group 5 were conducted using the setup in Fig. 2c corresponding to the fracturing within layered rocks in the heterogeneous stress and strain fields and jointing in sedimentary basins as described in the Introduction.

Group 5: Fracturing of a thick inviscid elastoplastic layer embedded between the stretching elastic layers.

Figs. 9a–e show four stages (columns 1 to 4) of the evolution of strain localization and fracture within the elastoplastic layer (the elastic layer is not shown) in five models with different Δz and ε^0 given in the figure caption. In the models in Figs. 9a–c, Δz and ε^0 are related by Eq. (8). The results are therefore supposed to be the same or close. This is indeed the case for the models with higher resolution $\Delta z = 1.25$ mm and $\Delta z = 2.5$ mm respectively in Figs. 9a and 9b, but the model in Fig. 9c with $\Delta z = 5$ mm shows more brittle behavior, with the fracture cutting through the entire layer at deformation stage 4 characterized by the same for all the models ε_{xx} value. This is not surprising as the response of the models becomes Δz–independent for Δz lower than a certain value. For the one-layer models, this value is around 2.5 mm (Fig. 8e), which is close to that following from Figs. 9a–c for the three-layer models that are characterized by different sizes and loading conditions (compared to one-layer models). For $\Delta z > 2.5$ mm, the stress reduction with the ε_{xx} increase is more rapid than for the models with smaller Δz as is seen in Fig. 8e. Therefore, the hardening modulus is more negative, and the fracture energy is smaller. To approach these parameters to the models with higher resolution, we increase ε^0 from 0.02 in Fig. 9c to 0.022 in Fig. 9d. The stress-strain curve for this ε^0 in one-layer models is closer to the curves for higher model resolution (Fig. 9f), and the strain localization and fracture processes in the three-layer model (Fig. 9d) approach those in Figs. 9a, b with higher resolution. In the lowest resolution model in Fig. 9e ($\Delta z = 10$ mm), $\varepsilon^0 = 0.012$ instead of 0.01 following from (8), for which the hardening modulus in the one-layer model is too negative (Fig. 9f). For $\varepsilon^0 = 0.012$, the $\sigma_{xx}(\varepsilon_{xx})$ curve is closer to those for smaller Δz (Fig. 9f). The result of strain localization and fracture in Fig. 9e4 is closer to that in higher resolution models in Figs. 9a4, b4, and d4 as well. The difference between all these models is obviously in the d_0 values, but also in the onset of strain localization near the layer interfaces. In Fig. 9a2, one can see many (14) deformation bands, and in Fig. 9e2, none, but this has very little effect on the final result. Note that the material damage at stage 2 is very small; the σ_t reduction is only ~1% of its initial value σ_t^0.

Group 6: Influence of the viscosity (regularization) on the evolution of strain localization and fracture in the layered models.

The setup and presentation of the results in Fig 10 are the same as for the models of the previous group. All models have the same $\Delta z = 2.5$ mm and $\varepsilon^0 = 0.04$. They differ only in the γ value: in Fig. 10a, which is the same as Fig. 9b, $\gamma = \infty$ and in Figs. 10b and 10c, γ is 0.15 and 0.01, respectively. One can see that in Fig. 10b2, the inelastic deformation is more diffuse, and there are fewer deformation bands than in Fig. 10a2, although the fracture evolution/propagation is practically the same at all stages. In the model in Fig. 10c, the

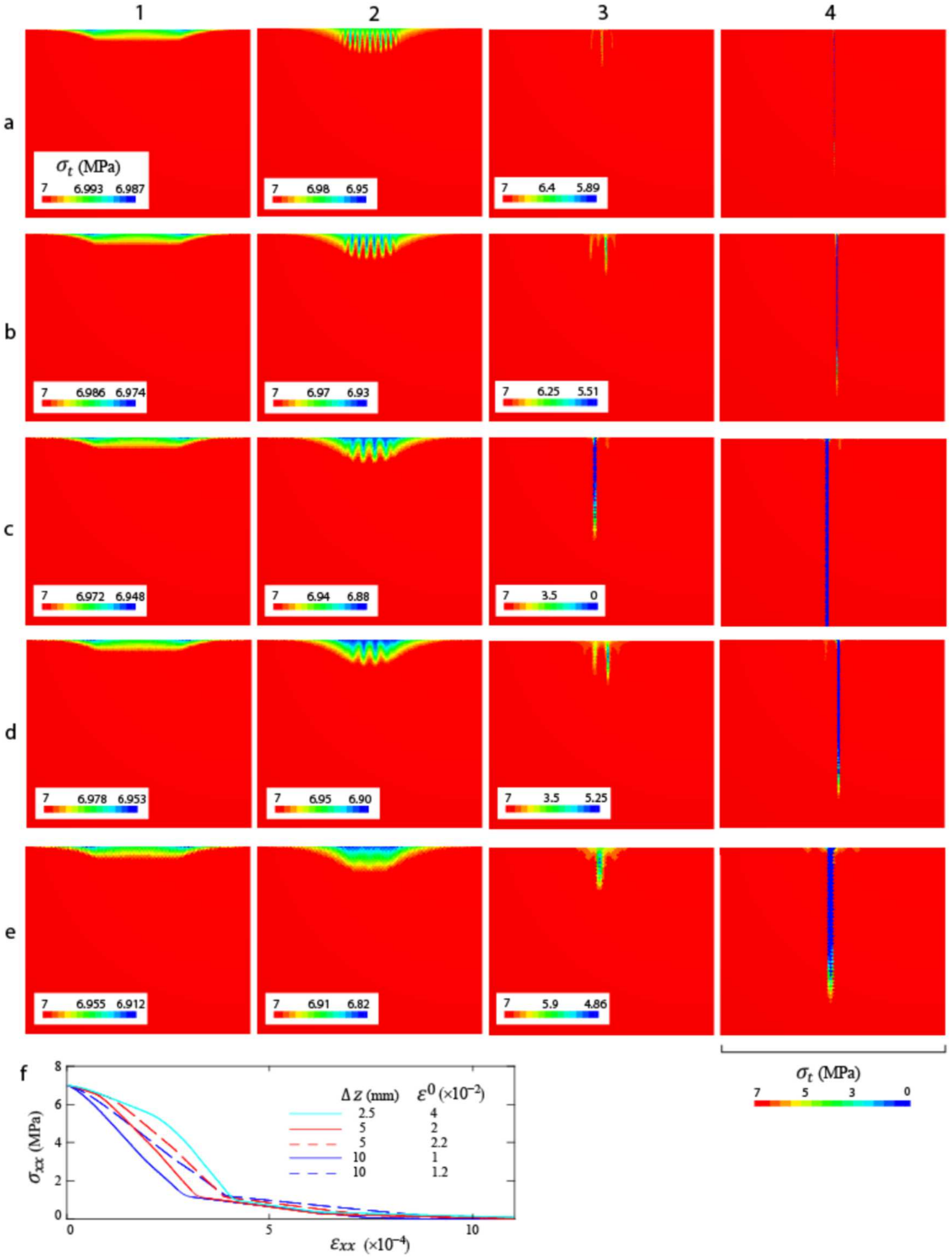

Figure 9. Group 5. Four evolutionary stages (columns 1 to 4) of strain localization and fracture in five 3-layer inviscid models (lines a to e) with double brick-wedge grids for layer 2; only this layer (its half, Fig. 2c) is shown. The models differ only by Δz and ε^0; in (a to c), they are related by Eq. (8): (a) $\Delta z = 1.25$ mm, $\varepsilon^0 = 0.08$; (b) $\Delta z = 2.5$ mm, $\varepsilon^0 = 0.04$; (c) $\Delta z = 5$ mm, $\varepsilon^0 = 0.02$. In (d), $\Delta z = 5$ mm, $\varepsilon^0 = 0.022$, and in (e), $\Delta z = 10$ mm, $\varepsilon^0 = 0.012$. The deformation stages shown (columns 1 to 4) correspond respectively to ε_{xx} of -6×10^{-4}, -9×10^{-4}, -2.1×10^{-3}, and -6×10^{-3}. (f) The stress-strain curves obtained from one-layer models for the same Δz and ε^0 as in the models a to e in this figure (the solid-line curves are the same as the corresponding curves in Fig. 8e).

viscous effect is the highest, and therefore there is no band initiation at stage 2 at all. It occurs only at stage 3, and so, the resulting fracture propagates over a much shorter distance. This fracture propagates over the same distance as in other models at larger ε_{xx}.

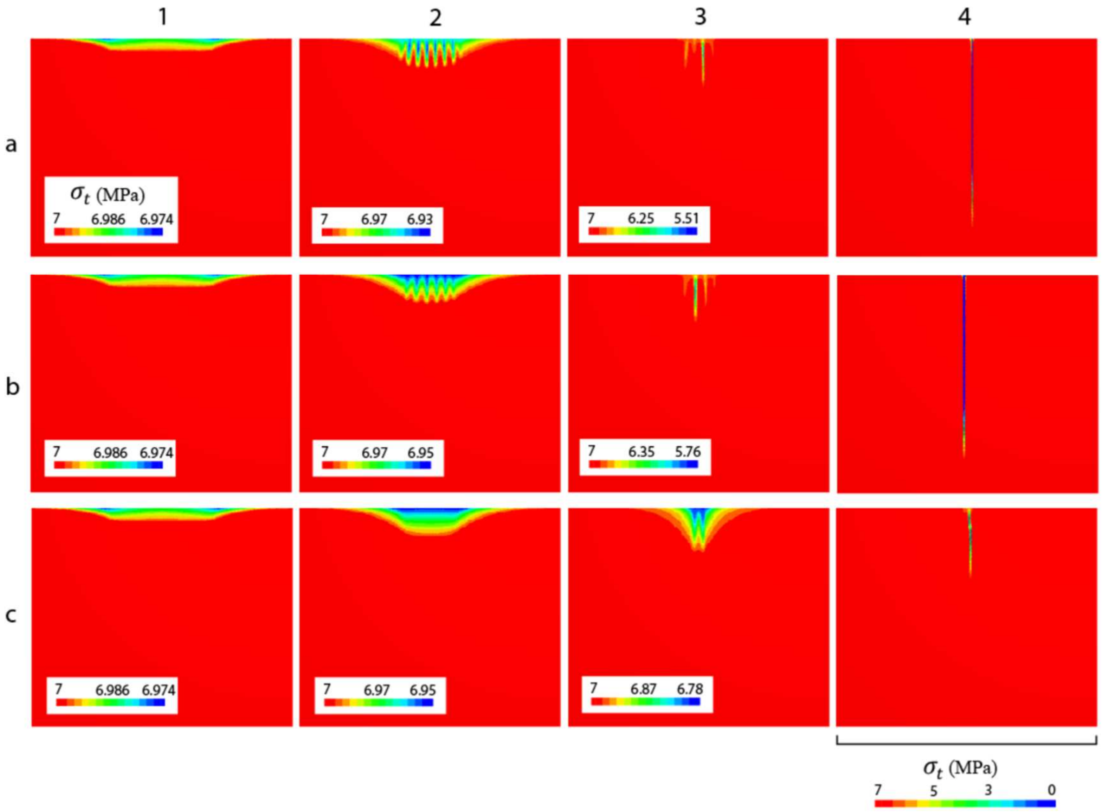

Figure 10. Group 6. Four evolutionary stages (columns 1 to 4) of strain localization and fracture in three 3-layer models (lines a to c) with double brick-wedge grids for the shown layer 2. The models differ only in the γ value: it is ∞, 0.15, and 0.01 in (a, b, and c), respectively. In all models $\Delta z = 2.5$ mm, $\varepsilon^0 = 0.04$; the deformation stages (1 to 4) correspond to the same ε_{xx} values as in the previous figure (see caption of Fig. 9).

6 Discussion

The width d_R of deformation localization bands in rocks at the origin of the faults and fractures is typically less than a fraction of a millimeter (subscript R stands for real/natural). Numerical models of deformation banding with the numerical size of $N = 10^7$ can be qualified as large or even very large. If size l of the modeled object (rock mass or geological structure) is 10 m, then the numerical element (zone) size is $\Delta z = l/\sqrt[3]{N}$ =4.6 cm for the indicated N value. The width of deformation bands d_M in the numerical models is typically larger than Δz and hence much larger than d_R, $d_M >> d_R$ (subscript M is for model). Since l can be hundreds of meters and kilometers, it is impossible to obtain deformation bands with realistic widths in most cases. Therefore, the convergence of the band thickness in numerical models like those in this study to a certain value using regularization procedures has a limited sense since this value will be very far from a realistic one anyway. On the other hand, such a convergence requires further model resolution refinement, as shown here. Therefore, one must accept that d_M is larger (much larger) than d_R and renounce the convergence of the band thickness with the model refinement. When using a viscous regularization like that in this paper, the introduction of a small viscosity (large γ) suffices to avoid the ill-posedness of the initial boundary value problem, although even this was not necessary for the models presented (compare, for instance, models in Figs. 10a and 10b). The effect of regularization should depend on the numerical code used and the details of numerical implementation. The dynamic relaxation procedure in FLAC3D, for example, provides a very diffusive integration scheme allowing to avoid the elastic structural snap backs during localization for any model refinement.

Since $d_M \neq d_R$, the constitutive model used in the numerical simulations cannot be exactly the same as that corresponding to natural material and defined from experimental data. It should be calibrated so that the energy dissipation during deformation localization and fracturing in the model is the same as in nature/experiment. Following Eq. (8), this means that ε^0 in the model (ε_M^0) should be related to the corresponding value ε_R^0 for nature as $\varepsilon_R^0/\varepsilon_M^0 \sim d_M/d_R$.

The models in Figs. 9 and 10 correspond to a step in the sequential fracture infill in a competent layer sandwiched between incompetent layers when a new joint forms between two previously formed ones. The fracture initiation is preceded by the defused (stage 1 in Figs. 9 and 10) and then localized inelastic straining or damage within several initial pure dilation bands (stages 2 to 3), whose number depends on the model resolution (Fig. 9) and viscosity (Fig. 10). It remains unclear if these bands do form in reality and, if yes, how many they are. They can hardly be detected experimentally given a very low degree of material damage within these bands (the strength reduction there does not exceed ~1%). The number of the bands in the numerical models does not impact the following fracture initiation and propagation processes. Therefore, the inelastic strain in the central oval zones near the layer interfaces (stage 2 in Figs. 9 and 10) can be considered diffusive until its definitive localization within a propagating band (stage 3) evolving to fracture initiation and propagation from the layer interface to the layer center (stage 4). Note that both geological observations ((Helgeson and Aydin, 1991; Savalli and Engelder, 2005; de Joussineau et al., 2005)) and experimental studies (Jorand et al., 2012; Chemenda, 2019) confirm that the fractures typically initiate from the interfaces of the fractured layer.

The models in Figs. 9 and 10 allow us to appreciate the limits of the most common tool used to analyze and predict the jointing in the rocks, Linear Elastic Fracture Mechanics. This theory implicitly assumes inelastic straining only in a very small zone at the tip of the imposed initial crack or seed oriented in a "right" (vertical in the context of Figs. 9 and 10) direction. In the modeling approach proposed here, the initial defect or weak zone is not imposed but formed with the orientation defined by the local stress field.

7 Conclusions

The fracturing of layered rocks with contrasting mechanical properties typical for sedimentary piles (basins) occurs in the brittle (competent) layers due to the tangential tractions generated at the frictional-cohesive interfaces between the adjacent layers. The fracturing process starts from inelastic straining or damage that should localize at a certain loading stage, leading to the fracture initiation. The details of this process were not clear and were frequently omitted in the models by introducing the initial microcracks (seeds) with certain lengths and orientations. Here we focus on these details and show for the first time that after initial elastic loading, the competent elastoplastic layer sandwiched between incompetent (less brittle) layers undergoes inelastic straining (damage) locally in the vicinity of the layer interfaces. This damage is first distributed and then localizes into narrow pure dilation bands where it is strongly accelerated and results in complete material failure and fracture initiation. Short initial fractures corresponding to the narrow bands of failed material are normal to the least local stress. They then propagate from the interfaces to the layer center with further extension, which agrees with geological observations and experimental studies. Since deformation localization is a bifurcation phenomenon, its numerical models are mesh-dependent and require an enrichment to eliminate or reduce this dependence. This issue is the subject of a careful study here with two regularization approaches. One is to ensure the same energy dissipation within the deformation/fracture bands for different mesh sizes Δz (hence different band widths in the models) by integrating Δz into the constitutive formulation. The classical viscous regularization applied allows to avoid the ill-posedness of the initial boundary value problem, although it has little effect on the results. The orientation of the deformation bands and the resulting fractures is defined by the constitutive low and stress orientation. However, in the numerical model it is also affected by the mesh geometry and notably by the grid lines. This effect was strongly reduced using double brick-wedge grids. The proposed modeling approach can be used for natural or induced fracture modeling in various contexts.

CRediT authorship contribution statement

Alexandre Chemenda: Conceptualization, Methodology, Software, Writing. Riad Hassani: Methodology, Software, Writing - review & editing. Jinyang Fan: Investigation, Writing - review & editing.

Declaration of Competing Interest

The authors declare that they have no known competing financial interests or personal relationships that could have appeared to influence the work reported in this paper.

Acknowledgments

This work has been supported by the French government through the UCAJEDI Investments in the Future project managed by the National Research Agency (ANR) with the reference number ANR-15-IDEX-01, by the BQR Geoazur 2020 grant, and INSU Tellus Program.

References

Bai, T., & Pollard, D. D., 2000. Closely spaced fractures in layered rocks: initiation mechanism and propagation kinematics. *Journal of Structural Geology*, *22*(10), 1409-1425. https://doi.org/10.1016/S0191-8141(00)00062-6

Bao, H., Zhai, Y., Lan, H., Zhang, K., Qi, Q., & Yan, C., 2019. Distribution characteristics and controlling factors of vertical joint spacing in sand-mud interbedded strata. *Journal of Structural Geology*, *128*, 103886.

Carosio, A., Willam, K., & Etse, G., 2000). On the consistency of viscoplastic formulations. *International Journal of Solids and Structures*, *37*(48-50), 7349-7369.

Chemenda, A. I., 2019. Origin of regular networks of joints: experimental constraints, theoretical background, and numerical modeling. *Journal of Geophysical Research: Solid Earth*, *124*(8), 9164-9181. https://doi.org/10.1029/2019JB017454

Chemenda, A. I., Lamarche, J., Matonti, C., Bazalgette, L., & Richard, P., 2021. Origin of strong nonlinear dependence of fracture (joint) spacing on bed thickness in layered rocks: mechanical analysis and modeling. *Journal of Geophysical Research: Solid Earth*, *126*(3), e2020JB020656.

Chen, Z., & Schreyer, H. L., 1987. Simulation of soil-concrete interfaces with nonlocal constitutive models. *Journal of engineering mechanics*, *113*(11), 1665-1677. https://doi.org/10.1061/(ASCE)0733-9399(1987)113:11(1665)

Cherepanov, G. P., 1997. On the origin of joints in sedimentary rocks. In *ICF 9-Sydney, Australia-1997*.

Cilona, A., Aydin, A., Likerman, J., Parker, B., & Cherry, J., 2016. Structural and statistical characterization of joints and multi-scale faults in an alternating sandstone and shale turbidite sequence at the Santa Susana Field Laboratory: Implications for their effects on groundwater flow and contaminant transport. *Journal of Structural Geology*, *85*, 95-114.

Das, A., Nguyen, G. D., & Einav, I., 2013). The propagation of compaction bands in porous rocks based on breakage mechanics. *Journal of Geophysical Research: Solid Earth*, *118*(5), 2049-2066.

de Joussineau, G., Bazalgette, L., Petit, J. P., & Lopez, M., 2005. Morphology, intersections, and syn/late-diagenetic origin of vein networks in pelites of the Lodève Permian Basin, Southern France. *Journal of Structural Geology*, *27*(1), 67-87. https://doi.org/10.1016/j.jsg.2004.06.016

de Joussineau, G., & Petit, J. P., 2021). Mechanical insights into the development of fracture corridors in layered rocks. *Journal of Structural Geology*, *144*, 104278.

Duretz, T., de Borst, R., & Le Pourhiet, L., 2019). Finite thickness of shear bands in frictional viscoplasticity and implications for lithosphere dynamics. *Geochemistry, Geophysics, Geosystems*, *20*(11 5598-5616.

Duvaut, G., & Lions, J. L., 1972. Les inéquations en mécanique et en physique. Dunod, Paris, 1972. *Travaux et Recherches Mathématiques*, *21*.

Engelder, T., Gross, M. R., & Pinkerton, P., 1997. An analysis of joint development in thick sandstone beds of the Elk Basin anticline. Montana-Wyoming: Fractured reservoirs: Characterization and modeling: Denver, Colorado, Rocky Mountain Association of Geologists, 1-18.

Gross, M. R., 1993. The origin and spacing of cross joints: examples from the Monterey Formation, Santa Barbara Coastline, California. *Journal of Structural Geology*, *15*(6), 737-751. https://doi.org/10.1016/0191-8141(93)90059-J

Gross, M. R., Fischer, M. P., Engelder, T., & Greenfield, R. J., 1995. Factors controlling joint spacing in interbedded sedimentary rocks: integrating numerical models with field observations from the Monterey Formation, USA. *Geological Society, London, Special Publications*, *92*(1), 215-233.. https://doi.org/10.1144/GSL.SP.1995.092.01.12

Guo, L., Latham, J. P., & Xiang, J., 2017. A numerical study of fracture spacing and through-going fracture formation in layered rocks. International Journal of Solids and Structures, 110, 44-57. https://doi.org/10.1016/j.ijsolstr.2017.02.004

Heeres, O. M., Suiker, A. S., & de Borst, R., 2002. A comparison between the Perzyna viscoplastic model and the consistency viscoplastic model. *European Journal of Mechanics-A/Solids*, *21*(1), 1-12.

Helgeson, D. E., & Aydin, A., 1991. Characteristics of joint propagation across layer interfaces in sedimentary rocks. *Journal of Structural Geology*, *13*(8), 897-911. https://doi.org/10.1016/0191-8141(91)90085-W

Hobbs, D. W., 1967. The formation of tension joints in sedimentary rocks: an explanation. *Geological Magazine*, *104*(6), 550-556. https://doi.org/10.1017/S0016756800050226

Huang, Q., & Angelier, J., 1989. Fracture spacing and its relation to bed thickness. *Geological Magazine*, *126*(4), 355-362. https://doi.org/10.1017/S0016756800006555

Itasca., 2021. Fast Lagrangian analysis of continua in 3-dimensions, version 7.0, manual. *Itasca, Minnesota.* http://docs.itascacg.com/flac3d700/flac3d/docproject/source/flac3dhome.html

Ji, S., Zhu, Z., & Wang, Z., 1998. Relationship between joint spacing and bed thickness in sedimentary rocks: effects of interbed slip. *Geological Magazine*, *135*(5), 637-655. https://doi.org/10.1017/S0016756898001459

Ji, S., Li, L., & Marcotte, D., 2021. Power-law relationship between joint spacing and bed thickness in sedimentary rocks and implications for layered rock mechanics. *Journal of Structural Geology*, *150*, 104413.

Jorand, C., Chemenda, A. I., & Petit, J. P., 2012. Formation of parallel joint sets and shear band/fracture networks in physical models. *Tectonophysics*, *581*, 84-92. https://doi.org/10.1016/j.tecto.2011.11.021

La Bruna, V., Lamarche, J., Agosta, F., Rustichelli, A., Giuffrida, A., Salardon, R., & Marié, L., 2020. Structural diagenesis of shallow platform carbonates: Role of early embrittlement on fracture setting and distribution, case study of Monte Alpi, Southern Apennines, Italy). *Journal of Structural Geology*, *131*, 103940. doi:https://doi.org/10.1016/j.jsg.2018.05.018

Ladeira, F. L., & Price, N. J., 1981. Relationship between fracture spacing and bed thickness. *Journal of Structural Geology*, *3*(2), 179-183. https://doi.org/10.1016/0191-8141(81)90013-4

Lavenu, A. P., & Lamarche, J., 2018. What controls diffuse fractures in platform carbonates? Insights from Provence, France) and Apulia, Italy). *Journal of Structural Geology*, *108*, 94-107. https://doi.org/10.1016/j.jsg.2017.05.011

Levi, T., Avni, Y., & Bahat, D., 2019. Evolution of the stress field near the Arava basin located along the Dead Sea Fault system as revealed by joint sets. *Journal of Structural Geology*, *128*, 103876.

Li, L. C., Tang, C. A., & Wang, S. Y., 2012. A numerical investigation of fracture infilling and spacing in layered rocks subjected to hydro-mechanical loading. *Rock mechanics and rock engineering*, *45*(5), 753-765. DOI 10.1007/s00603-011-0194-x

Loret, B., & Prevost, J. H., 1990. Dynamic strain localization in elasto-(visco-) plastic solids, Part 1. General formulation and one-dimensional examples. *Computer Methods in Applied Mechanics and Engineering*, *83*(3), 247-273.

McQuillan, H., 1973. Small-scale fracture density in Asmari Formation of southwest Iran and its relation to bed thickness and structural setting. *AAPG Bulletin*, 57(12), 2367-2385. https://doi.org/10.1306/83D9131C-16C7-11D7-8645000102C1865D

Olson, J. E., Laubach, S. E., & Lander, R. H., 2009. Natural fracture characterization in tight gas sandstones: Integrating mechanics and diagenesis. *AAPG Bulletin*, *93*(11 1535-1549. DOI:10.1306/08110909100

Ottosen, N. S., & Runesson, K., 1991. Properties of discontinuous bifurcation solutions in elasto-plasticity. *International Journal of Solids and Structures*, *27*(4), 401-421. https://doi.org/10.1016/0020-7683(91)90131-X

Paterson, M. S., & Wong, T. F., 2005. *Experimental rock deformation-the brittle field.* Springer Science & Business Media.

Perzyna, P., 1966. Fundamental problems in viscoplasticity. In *Advances in applied mechanics* (Vol. 9, pp. 243-377). Elsevier.

Pijaudier-Cabot, G., & Bažant, Z. P., 1987. Nonlocal damage theory. *Journal of engineering mechanics*, *113*(10), 1512-1533. https://doi.org/10.1061/(ASCE)0733-9399(1987)113:10(1512)

Poh, L. H., & Swaddiwudhipong, S., 2009. Over-nonlocal gradient enhanced plastic-damage model for concrete. *International Journal of Solids and Structures*, *46*(25-26), 4369-4378.

Pollard, D. D., & Aydin, A., 1988. Progress in understanding jointing over the past century. *Geological Society of America Bulletin*, *100*(8), 1181-1204. https://doi.org/10.1130/0016-7606(1988)100<1181:PIUJOT>2.3.CO;2

Price, N. J., 1966. *Fault and joint development: in brittle and semi-brittle rock.* Pergamon Press Ltd., Oxford.

Narr, W., & Suppe, J., 1991. Joint spacing in sedimentary rocks. *Journal of Structural Geology*, 13(9), 1037-1048. https://doi.org/10.1016/0191-8141(91)90055-N

Needleman, A., 1988. Material rate dependence and mesh sensitivity in localization problems. *Computer methods in applied mechanics and engineering*, *67*(1), 69-85. https://doi.org/10.1016/0045-7825(88)90069-2

Nguyen, G. D., & Korsunsky, A. M., 2008. Development of an approach to constitutive modelling of concrete: isotropic damage coupled with plasticity. *International Journal of Solids and Structures*, *45*(20), 5483-5501. https://doi.org/10.1016/j.ijsolstr.2008.05.029

Rice, J. R., 1976. The localization of plastic deformation. In W.T. Koiter (Ed), *Theoretical and Applied Mechanics* (Proceedings of the 14th International Congress on Theoretical and Applied Mechanics, Delft, Vol. 1, pp. 207-220). North-Holland Publishing Co.

Rudnicki, J. W., & Rice, J. R., 1975. Conditions for the localization of deformation in pressure-sensitive dilatant materials. *Journal of the Mechanics and Physics of Solids*, *23*(6), 371-394. https://doi.org/10.1016/0022-5096(75)90001-0

Ruf, J. C., Rust, K. A., & Engelder, T., 1998. Investigating the effect of mechanical discontinuities on joint spacing. *Tectonophysics*, *295*(1-2), 245-257.

Rustichelli, A., Agosta, F., Tondi, E., & Spina, V., 2013. Spacing and distribution of bed-perpendicular joints throughout layered, shallow-marine carbonates (Granada Basin, southern Spain). *Tectonophysics*, *582*, 188-204.

Sagy, A., & Reches, Z. E., 2006. Joint intensity in layered rocks: The unsaturated, saturated, supersaturated, and clustered classes. *Israel Journal of Earth Sciences*, *55*(1).

Savalli, L., & Engelder, T., 2005. Mechanisms controlling rupture shape during subcritical growth of joints in layered rocks. *Geological Society of America Bulletin*, *117*(3-4. 436-449. https://doi.org/10.1130/B25368.1

Schöpfer, M. P., Arslan, A., Walsh, J. J., & Childs, C., 2011. Reconciliation of contrasting theories for fracture spacing in layered rocks. *Journal of Structural Geology*, *33*(4), 551-565. https://doi.org/10.1016/j.jsg.2011.01.008

Segall, P., & Pollard, D. D., 1983. Joint formation in granitic rock of the Sierra Nevada. *Geological Society of America Bulletin*, *94*(5), 563-575. https://doi.org/10.1130/0016-7606(1983)94<563:JFIGRO>2.0.CO;2

Shahin, G., Papazoglou, A., Marinelli, F., & Buscarnera, G., 2019. Simulation of localized compaction in Tuffeau de Maastricht based on evidence from X-ray tomography. *International Journal of Rock Mechanics and Mining Sciences*, *121*, 104039. A

Shahin, G., Torabi, A., Rudnicki, J., & Buscarnera, G., 2021. The Role of Stratigraphy and Loading History in Generating Complex Compaction Bands in Idealized Field-Scale Settings. *Journal of Geophysical Research: Solid Earth*, *126*(2), e2020JB020452.

Simo, J. C., Kennedy, J. G., & Govindjee, S., 1988. Non-smooth multisurface plasticity and viscoplasticity. Loading/unloading conditions and numerical algorithms. *International Journal for Numerical Methods in Engineering*, *26*(10), 2161-2185.

Vardoulakis, I., 1989. Shear-banding and liquefaction in granular materials on the basis of a Cosserat continuum theory. *Ingenieur-Archiv*, *59*(2), 106-113. https://doi.org/10.1007/BF00532250

Wang, W. M., Sluys, L. J., & De Borst, R., 1997. Viscoplasticity for instabilities due to strain softening and strain-rate softening. *International Journal for Numerical Methods in Engineering*, *40*(20), 3839-3864.

Figure captions

Figure 1. Field examples of layered and fractured sedimentary rocks. (a) Alternating incompetent (mudrocks) and fractured competent (limestone) layers in Lilstock Bay, Somerset, UK (rock hammer for scale) from Schöpfer et al. (2011). (b) Thick densely fractured Urgonian limestone layers; Cassis, Provence, SE France from Chemenda et al. (2021).

Figure 2. Setup of 3-layer models. (a) Series of alternating incompetent (pink) and competent (blue) layers. (b) An elementary (repeating) element of this series which corresponds to the complete three-layer modeling setup. (c) A half-symmetry modeling setup, with thicknesses of layers 1 and 2 being $T_1/2$ and $T/2$, respectively. V_x and V_z are the velocities applied in the corresponding directions to layers 1 and 3. V_x causes deformation and fracturing of layer 2 and V_z is to maintain constant average vertical (lithostatic) stress at the horizontal model boundaries. The y-normal model boundaries are fixed in the y-direction. The layers are separated by cohesive-frictional interfaces. The models are pre-stressed in the y- and z-directions as indicated below. Layers 1 and 3 are purely elastic and layer 2 is elastoplastic. $T_1 = T_1 = 0.2$ m, $T = 1$ m, and $L = 0.6$ m.

Figure 3. Composite yield surface $\sigma_3(\sigma_1, \varepsilon^p)$. (1) Tensile failure. (2) Shear failure. (3) Post failure (after complete failure). (4) Shows a zero-level of σ_3. The red point (circle) corresponds to the initial stresses $\sigma_1 = \sigma_{xx}^{ini}$ and $\sigma_3 = 0$ applied to the models.

Figure 4. Setup of one-layer models (a) and grid geometries used (b to d). (b and c) Brick- and wedge-shaped grids, respectively. (d) Double-layer sheet grid, with the attached brick and wedge-shaped grids. $T = 0.1$ m, and $L = 0.2$ m.

Figure 5. Group 1. Evolution of strain localization and fracture (stages/columns 1 to 5) in three models (a to c) differing only by the γ value: in (a), $\gamma = \infty$; in (b), $\gamma = 0.1$, and in (c), $\gamma = 0.01$. Deformation stages 1 to 5 correspond to ε_{xx} equal to -5×10^{-6}, -1.5×10^{-5}, -6×10^{-5}, -4.5×10^{-4}, and -7.8×10^{-4}, respectively. $\Delta z = 5$ mm and $\varepsilon^0 = 0.02$. All the models have wedge-shaped grids shown in Fig. 4c.

Figure 6. Group 2. Impact of the grid geometry, resolution, and the regularization parameter γ on the dilation banding and structural stress-strain response. Final stages of strain localization and fracture are shown for five models with brick- (a) and wedge-shaped (b) meshes, respectively. The resolution of the models in columns 1 and 3 is $\Delta z = 5$ mm, in columns 2 and 4, 2.5 mm, and in column 5, 1.25 mm. In columns 1 and 2, $\gamma = \infty$, and in columns 3 to 5, $\gamma = 1 \times 10^{-3}$. (c to h) Nominal stress-strain curves $\sigma_{xx}(\varepsilon_{xx})$ in the presented models. Since the models are pre-stressed to σ_{xx} close to $-\sigma_t^0$, the curves start near the initial failure (yield) point except in (c), where the elastic loading stage (segment) is added to the curves in (d). The curves in (d and e) are respectively for the models in columns 1 and 2 (curve (c) is for column 1 as well). Curves in (g), are for the regularized brick-shaped models in (a3 to a5) with different resolutions indicated on the plot. (h) Curves for the regularized models with the brick, wedge, and double brick-wedge grids corresponding to the curves of different colors as indicated in (h). Solid curves are for $\Delta z = 1.25$ mm, and the dashed ones, for $\Delta z = 2.5$ mm.

Figure 7. Group 3. Final stages of strain localization and fracture in the models with brick (a), wedge (b), and double brick-wedge (c) grids. The columns 1 to 3 correspond to different orientations of the initial stress axes defined by angle ψ between σ_1 (shown by the white dashed lines) and the vertical; ψ is 0°, 15°, and 30° in columns 1, 2, and 3, correspondingly. In column 4, $\psi = 30°$. The rotation of the initial stress axes is achieved by imposing the

corresponding normal and shear initial and boundary stresses. Models in columns 1 to 3 are inviscid ($\gamma = \infty$), and in column 4, $\gamma = 1 \times 10^{-3}$. In all models $\Delta z = 2.5$ mm and $\varepsilon^0 = 0.02$.

Figure 8. Group 4. (a to d) Final stages of strain localization and fracture in the inviscid models with double brick-wedge grids and different ε^0 and Δz related by Eq. (8): (a) $\varepsilon^0 = 0.01$ and $\Delta z = 10$ mm; (b) $\varepsilon^0 = 0.02$ and $\Delta z = 5$ mm; (c) $\varepsilon^0 = 0.04$ and $\Delta z = 2.5$ mm; (d) $\varepsilon^0 = 0.08$ and $\Delta z = 1.25$ mm. (e) Nominal stress-strain curves from the models presented and other similar ones with different Δz (and hence ε^0): for (1) $\Delta z = 0.625$ mm; (2) $\Delta z = 1.25$ mm; (3) $\Delta z = 2$ mm; (4) $\Delta z = 2.5$ mm; (5) $\Delta z = 2.7$ mm; (6) $\Delta z = 5$ mm; (7) $\Delta z = 10$ mm. (f) Nominal stress-strain curves obtained from other models with $\Delta z = 1.25$ mm, $\varepsilon^0 = 0.08$, and different γ indicated on this figure.

Figure 9. Group 5. Four evolutionary stages (columns 1 to 4) of strain localization and fracture in five 3-layer inviscid models (lines a to e) with double brick-wedge grids for layer 2; only this layer (its half, Fig. 2c) is shown. The models differ only by Δz and ε^0; in (a to c), they are related by Eq. (8): (a) $\Delta z = 1.25$ mm, $\varepsilon^0 = 0.08$; (b) $\Delta z = 2.5$ mm, $\varepsilon^0 = 0.04$; (c) $\Delta z = 5$ mm, $\varepsilon^0 = 0.02$. In (d), $\Delta z = 5$ mm, $\varepsilon^0 = 0.022$, and in (e), $\Delta z = 10$ mm, $\varepsilon^0 = 0.012$. The deformation stages shown (columns 1 to 4) correspond respectively to ε_{xx} of -6×10^{-4}, -9×10^{-4}, -2.1×10^{-3}, and -6×10^{-3}. (f) The stress-strain curves obtained from one-layer models for the same Δz and ε^0 as in the models a to e in this figure (the solid-line curves are the same as the corresponding curves in Fig. 8e).

Figure 10. Group 6. Four evolutionary stages (columns 1 to 4) of strain localization and fracture in three 3-layer models (lines a to c) with double brick-wedge grids for the shown layer 2. The models differ only in the γ value: it is ∞, 0.15, and 0.01 in (a, b, and c), respectively. In all models $\Delta z = 2.5$ mm, $\varepsilon^0 = 0.04$; the deformation stages (1 to 4) correspond to the same ε_{xx} values as in the previous figure (see caption of Fig. 9).

Nomenclature

E	Young's modulus
ν	Poisson's ratio
G	Shear modulus
K	Bulk modulus
ε^p	Accumulated inelastic (plastic) volume strain
$\sigma_t(\ \varepsilon^p)$	Tensile strength which is function of ε^p
σ_t^0	Initial (at $\varepsilon^p = 0$) tensile strength
$\sigma_c(\varepsilon^p)$	Unconfined (uniaxial) compression strength
σ_c^0	Initial value of σ_c
α_c, β_c	Material parameters in equations (1) and (4)
β_c^0	Initial value of β_c
σ_{ij}	Stress tensor, $i, j = 1,2,3$
ε_{ij}	Strain tensor
σ_i	Principal effective stresses, compression positive, $i = 1,2,3$
$\sigma_{int}(\varepsilon^p)$	Equal to the major stress σ_1 at the intersection of tensile and shear yield envelopes in the (σ_1, σ_3) space (equation (2))
σ_{int}^0	Initial value of σ_{int}
β	Dilatancy factor (equation (6))
ε^0	Inelastic volume strain at which σ_t, σ_c, σ_{int}, and β reach zero
ρ	Density
k_n and k_s	Normal and shear stiffnesses of the interfaces
x, y, z	Axes defined in Fig. 2
σ_{xx}, σ_{yy}, σ_{zz}	Horizontal and vertical (lithostatic) effective normal stresses

σ_{xx}^{ini}, σ_{yy}^{ini}, σ_{zz}^{ini}	Initial effective stresses in the numerical models
V_x and V_z	Rates applied to the model boundaries in the corresponding directions
τ^{int}	Shear stress along the interfaces between the layers
τ_0^{int}	Interface shear strength
c^{int}	Interface cohesion
μ^{int}	Interface friction coefficient
T_1, T_2, and T	Thicknesses of the layers defined in Figure 2a
L	Length of the models
S	Fracture spacing
ψ	angle between σ_1 and the vertical
σ_{xx} and ε_{xx}	Nominal horizontal tension stresses and extension strains, respectively
F, F_t, F_s	Yield functions defined in equations (1)
Φ, Φ_t, Φ_s	Plastic potential functions defined in equations (4)
η	Relaxation time, equation (10)
γ	Regularization (viscous) parameter, equation (12)
Δz	Numerical grid element (zone) size
d_0	Thickness of the deformation or fracture band in numerical models
Δd	Change of the width of dilation bands during extension of the models
C, $\tilde{\varepsilon}^0$	Defined in equation (8)